Soft Matter

PAPER

View Article Online
View Journal

Check for updates

Cite this: DOI: 10.1039/c9sm00677j

State diagram for wall adhesion of red blood cells in shear flow: from crawling to flipping†

Anil K. Dasanna, [ab] Dmitry A. Fedosov, [b] Gerhard Gompper [b] and Ulrich S. Schwarz *[a]

Red blood cells in shear flow show a variety of different shapes due to the complex interplay between hydrodynamics and membrane elasticity. Malaria-infected red blood cells become generally adhesive and less deformable. Adhesion to a substrate leads to a reduction in shape variability and to a flipping motion of the non-spherical shapes during the mid-stage of infection. Here, we present a complete state diagram for wall adhesion of red blood cells in shear flow obtained by simulations, using a particle-based mesoscale hydrodynamics approach, multiparticle collision dynamics. We find that cell flipping at a substrate is replaced by crawling beyond a critical shear rate, which increases with both membrane stiffness and viscosity contrast between the cytosol and suspending medium. This change in cell dynamics resembles the transition between tumbling and tank-treading for red blood cells in free shear flow. In the context of malaria infections, the flipping–crawling transition would strongly increase the adhesive interactions with the vascular endothelium, but might be suppressed by the combined effect of increased elasticity and viscosity contrast.

Received 2nd April 2019,
Accepted 18th June 2019

DOI: 10.1039/c9sm00677j

rsc.li/soft-matter-journal

Published on 19 June 2019. Downloaded by Ruprecht-Karls Universitat Heidelberg on 6/27/2019 10:20:37 AM.

1 Introduction

Adhesion is an essential element of the function of biological cells, *e.g.* as a prerequisite for migration or to achieve mechanical cohesion across a monolayer of endothelial cells. Both of these aspects play an important role in the processes of extravasation, for example when adhesive white blood cells leave the blood circulation to follow the signs of inflammation in the surrounding tissue.[1] In contrast, healthy red blood cells (RBCs) are not adhesive as their main function is to circulate passively within the vasculature and to distribute oxygen in the body by temporarily binding it to their hemoglobin. However, this situation changes dramatically when RBCs become infected by the malaria parasite, which uses them to shield itself from the immune system and to metabolize the hemoglobin.[2] The parasite makes infected RBCs (iRBCs) adhesive by establishing a system of adhesive knobs on the surface of iRBCs. This increases the residency time of parasites in the vasculature and protects iRBCs from clearance by the spleen. However, it also increases adhesive interactions with the endothelium and therefore, can lead to inflammation. Despite the high medical relevance of the adhesive interaction between iRBCs and the vascular endothelium, little is known about the exact nature of this interaction, partially due to a complex interplay between hydrodynamic flow and cellular characteristics such as the shape, elasticity, viscosity, and adhesion strength.

To understand the interaction between iRBCs and an adhesive substrate, it is helpful to consider the related case of white blood cells in more detail. Leukocyte adhesion in flow has been studied extensively, using both *in vitro* flow chamber experiments and computer simulations.[3] The initial capture of leukocytes from shear flow is mediated by binding of glycoprotein PSGL-1 to P-selectin on the endothelial cells, while further interactions between integrins and ICAM molecules lead to firm adhesion and migration of leukocytes.[4,5] It has been shown that the PSGL-1:P-selectin bond behaves like a catch-slip bond, meaning that bond lifetime increases till a threshold shear rate after which it decreases.[6] On the modeling side, adhesion-dynamics simulations of cells have been pioneered for rigid spherical particles homogeneously covered with adhesion receptors[7–9] and later extended to also include spatially resolved ligand and receptor positions.[10,11] These models predict dynamic states such as rolling adhesion, firm adhesion or transient adhesion as a function of model parameters, including on- and off-rates of receptor–ligand bonds as well as shear rate of the flow. Corresponding state diagrams have been determined from simulations over a wide range of model parameters. Further extensions of adhesion-dynamics simulations for leukocytes concern the role of cell deformability,

[a] BioQuant and Institute of Theoretical Physics, Heidelberg University, Heidelberg, Germany. E-mail: schwarz@thphys.uni-heidelberg.de
[b] Theoretical Soft Matter and Biophysics, Institute of Complex Systems and Institute for Advanced Simulation, Forschungszentrum Jülich, 52425 Jülich, Germany

† Electronic supplementary information (ESI) available: Videos of two different dynamics (*i.e.* flipping and crawling) of red blood cells adhered to a wall under shear flow. See DOI: 10.1039/c9sm00677j

Published on 19 June 2019. Downloaded by Ruprecht-Karls Universitat Heidelberg on 6/27/2019 10:20:37 AM.

which is essential to ensure a sufficiently large contact area.[12] However, rolling adhesion can also be suppressed by increased deformability, as this can lead to concave shapes in the contact region.[13]

Interestingly, the adhesive interaction of iRBCs with the endothelium strongly resembles that of leukocytes.[14] The deadliest form of human malaria is caused by the parasite *Plasmodium falciparum*. The blood stage of infection proceeds in three stages: ring (0–24 hours post infection), trophozoite (24–36 hpi), and schizont (40–48 hpi) stages. At the end of the schizont stage, iRBCs burst and release around 20 new parasites into the bloodstream, which then infect fresh RBCs. During the infectious cycle, iRBC develops thousands of adhesive protrusions on its surface, called knobs, starting in the late ring stage (around 15 hpi). Knobs were visualized with scanning electron microscopy[15] and atomic force microscopy.[16] Host-cell modification also includes membrane stiffness and shape of an iRBC. Using confocal microscopy, it was shown that an iRBC almost retains its discocyte shape till the early trophozoite stage, after which it gradually transforms into a spherical shape.[17,18] Using optical tweezers, it was shown that the shear modulus of iRBC increases by one order of magnitude, from around 5 $\mu N\ m^{-1}$ to around 50 $\mu N\ m^{-1}$.[19] PfEMP-1, the adhesive receptor produced by the parasite, resides at the knobs and can bind to the ligands at the endothelial cells such as ICAM-1 or CD36. It is believed that ICAM-1 participates in rolling of iRBCs, whereas CD36 is responsible for their firm adhesion, and that both of them work synergistically in iRBC cytoadhesion.[20–22] iRBCs with a non-spherical shape and the ability to deform under shear give rise to a complex adhesion dynamics. Using mesoscopic simulations,[23] it has been predicted that iRBCs flip under shear flow at physiological shear rates. Later, this was confirmed using flow chamber experiments and further simulations, correlating iRBC velocity and parasite position inside the cell.[24,25]

Despite these recent advances in understanding and simulating the adhesive interactions of iRBCs with a substrate,[26] a systematic investigation is still lacking of how the interplay of hydrodynamic flow, cell shape and deformability determines the interaction of RBCs with an adhesive substrate. Here, we present a comprehensive study of RBC adhesion, using the multiparticle collision dynamics (MPCD) method[27,28] for the fluid dynamics and triangulated networks[29–31] for the RBC membrane shape and deformability, and provide an adhesion state diagram with a special focus on the roles of membrane shear elasticity and hydrodynamic shear rate. As a main feature, we identify the transition between flipping and crawling (compare Fig. 1). While flipping implies a vertical movement of the geometrical center of the cell with respect to the wall, crawling defines a dynamic state in which this center keeps about the same height from the wall and the cell membrane rotates around it. Interestingly, these two dynamic states and the transition between them strongly resemble the tumbling and tank-treading of RBCs in unbounded shear flow.[32,33] While the first case corresponds to an elastic body (like a solid ellipsoid) moving in shear flow, the second is typical for a viscous body (like a fluid droplet) in shear flow. The latter is also similar to a viscous drop sliding down an inclined plane.[34] RBCs in free shear flow not only tumble and tank-tread, but also roll, swing, form trilobes and multilobes, depending on the shear rate and the viscosity contrast between the cytosol and suspending medium.[35] For iRBCs, however, substrate adhesion restricts the range of possible shapes in comparison to those in free shear flow. We show that flipping and crawling are the two main types of motion which should be expected in this case.

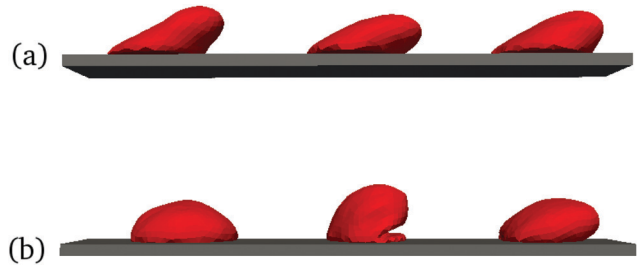

Fig. 1 Snapshots of a crawling (a) and a flipping (b) cell in shear flow (see also Movies S1 and S2, ESI†). The shear rate is $\dot{\gamma} = 460$ Hz ($\dot{\gamma}^* \simeq 430$). The shear moduli are 5 $\mu N\ m^{-1}$ and 25 $\mu N\ m^{-1}$ (or $\Gamma \simeq 2870$ and $\Gamma \simeq 14\,370$) for the crawling and the flipping cell, respectively. The increased elasticity effects a transition from crawling to flipping.

By using MPCD with angular momentum conservation, we are also able to investigate the effect of viscosity contrast on RBC adhesion and find that an increase in viscosity contrast shifts the transition to higher shear rates. This finding has a direct biological relevance, because iRBCs are characterized by an increased internal viscosity, which might suppress the flipping-to-crawling transition at physiological shear rates, in addition to the effect of increased membrane shear modulus. Together, these effects keep the adhesive interactions with the endothelium low, thus possibly avoiding a strong inflammatory response.

This article is organized as follows. First, we describe methods and models used in simulations. Then, we identify the different dynamic states using order parameters that help us to distinguish them. Consequently, we present the simulated state diagram as a function of shear rate and membrane shear modulus, and discuss the effect of viscosity contrast on the state diagram and RBC adhesion.

2 Methods and models

2.1 Multiparticle collision dynamics

Hydrodynamic interactions are implemented through the multiparticle collision dynamics (MPCD) approach, a technique which also incorporates thermal fluctuations.[27,28] We employ a MPCD version with the Andersen thermostat and angular momentum conservation (MPC-AT + a).[36–38] The MPCD fluid consists of point particles with mass m, position $\boldsymbol{r}(t)$ and velocity $\boldsymbol{v}(t)$. The particles are sorted into the cells of a cubic lattice with lattice constant a, which also sets the basic length scale in the system. The dynamics proceed in two steps: streaming and collision. Particles are moved ballistically during the streaming step as

$$\boldsymbol{r}_i(t + \Delta t_{cd}) = \boldsymbol{r}_i(t) + \boldsymbol{v}_i(t)\Delta t_{cd}, \quad (1)$$

Published on 19 June 2019. Downloaded by Ruprecht-Karls Universitat Heidelberg on 6/27/2019 10:20:37 AM.

where Δt_{cd} is the collision timestep. During the collision step, particle velocities are altered as

$$\boldsymbol{v}_i^{new} = \boldsymbol{v}_{cm} + \boldsymbol{v}_i^{ran} - (1/N_c)\sum_{j\in cell}\boldsymbol{v}_j^{ran} + \left[m\boldsymbol{I}^{-1}\sum_{j\in cell}\left\{\boldsymbol{r}_{j,c}\times\left(\boldsymbol{v}_j - \boldsymbol{v}_j^{ran}\right)\right\}\right]\times\boldsymbol{r}_{i,c}, \quad (2)$$

where $\boldsymbol{v}_{cm}$ is the center-of-mass velocity of the cell to which particle i belongs and $\boldsymbol{v}_i^{ran}$ is a thermal velocity drawn from Maxwell–Boltzmann distribution. The last term is the correction term for angular momentum conservation, where $\boldsymbol{I}$ is the moment of inertia tensor for all particles in the cell and $\boldsymbol{r}_{j,c} = \boldsymbol{r}_j - \boldsymbol{r}_{cm}$ is the position vector of particle j with respect to center of mass of the cell.

Viscosity of the fluid depends on the choice of collision timestep Δt_{cd}, mass m, and the particle density ρ. It has two contributions: kinetic viscosity η_{kin} which results from particle streaming, and collision viscosity η_{col} which results from the momentum transfer among the fluid particles during the collision step. The total fluid viscosity is $\eta = \eta_{kin} + \eta_{col}$. For large particle densities, the viscosity contributions are given by[36,37]

$$\eta_{kin} = \frac{\rho k_B T\Delta t_{cd}}{a^3}\left[\frac{\rho}{\rho - 5/4} - \frac{1}{2}\right], \quad (3)$$

$$\eta_{col} = \frac{m(\rho - 7/5)}{24a\Delta t_{cd}}. \quad (4)$$

For small collision timesteps Δt_{cd}, the kinetic viscosity η_{kin} can be neglected and the collision viscosity η_{col} provides main contribution to the total viscosity, *i.e.* $\eta \simeq \eta_{col}$.

2.2 Deformable RBC model

The RBC membrane is modeled as a two dimensional triangulated meshwork of springs.[29,30] The meshwork comprises $N = 751$ vertices with positions $\{\boldsymbol{r}_i\}$ and velocities $\{\boldsymbol{v}_i\}$.[31,39,40] Total number of edges is N_e and number of triangles is N_t. The total potential energy of the system is given by

$$V(\{x_i\}) = V_{in\text{-}plane} + V_{bend} + V_{area} + V_{vol}. \quad (5)$$

The first term is an in-plane elastic energy of the network,

$$V_{in\text{-}plane} = \sum_{i=1}^{N_e}\frac{k_B T\ell_m\left(3x_i^2 - 2x_i^3\right)}{4p(1 - x_i)} + \frac{k_p}{\ell_i}, \quad (6)$$

where the first part is a worm-like chain potential describing an attractive interaction and the second term is a short-ranged repulsive potential. In the first term, p is the persistence length, ℓ_i is the extension of edge i, ℓ_m the maximum edge extension, and $x_i = \ell_i/\ell_m$. In the second term, k_p is the force coefficient.

The second term in eqn (5) represents bending energy of the triangular mesh,

$$V_{bend} = \sum_{i=1}^{N_e}\kappa_b(1 - \cos(\theta_i - \theta_0)), \quad (7)$$

where κ_b is the bending coefficient, θ_i is the angle between two triangles having a common edge, and $\theta_0 \simeq 5.66^\circ$ is the preferred angle which depends on the mesh size.[31] The bending coefficient κ_b is related to the bending modulus κ_c of the Helfrich curvature-elasticity model[41] as $\kappa_b = (2/\sqrt{3})\kappa_c$.

The last two terms in eqn (5), V_{area} and V_{vol}, constrain surface area and volume of the RBC:

$$V_{area} = \frac{k_a(A - A_0)^2}{2A_0} + \sum_{i=1}^{N_t}\frac{k_d\left(A_i - A_i^0\right)^2}{2A_i^0}, \quad (8)$$

$$V_{vol} = \frac{k_v(V - V_0)^2}{2V_0},$$

where k_a, k_d and k_v are the constraint coefficients for total surface area A of the cell, local area A_i of each triangle, and total volume V of the cell, respectively. We choose these coefficients such that surface area and volume of the RBC fluctuate within 1% of their desired values (*i.e.* A_0, A_i^0, and V_0).

For a regular hexagonal network, shear modulus μ_0, Young's modulus Y, and Poisson's ratio ν are derived in terms of model parameters as[31,39]

$$\mu_0 = \frac{\sqrt{3}k_B T}{4p\ell_m x_0}\left(\frac{x_0}{2(1 - x_0)^3} - \frac{1}{4(1 - x_0)^2} + \frac{1}{4}\right) + \frac{\sqrt{3}k_p}{2\ell_0^2}, \quad (9)$$

$$Y = \frac{4K\mu_0}{K + \mu_0}, \quad (10)$$

$$\nu = \frac{K - \mu_0}{K + \mu_0}, \quad (11)$$

where $K = 2\mu_0 + k_a + k_d$ is the area compression modulus and $x_0 = \ell_0/\ell_m$ with an equilibrium length ℓ_0 of each edge. We employ a stress-free membrane model,[31,39] in which each edge has its own equilibrium length l_0^i set according to distances in the initial membrane triangulation. This also leads to individual values of the maximum extension $l_m^i = l_0^i x_0$ with $x_0 = 2.2$, the persistence length p_i, and the force coefficient k_p^i for each spring with a fixed μ_0. The Poisson's ratio ν is selected to be approximately 0.96, leading to a nearly incompressible membrane with $Y \simeq 4\mu_0$.

Solvent particles interact with the membrane in two ways: (i) membrane vertices are included in the collision step together with fluid particles and (ii) fluid particles are subject to bounce-back reflection at membrane triangular plaquettes. This means that internal and external fluids are separated and do not mix. Thus, distinct viscosities for the internal and external fluids (*i.e.* η_i and η_o) can be employed, allowing different viscosity contrasts $\lambda = \eta_i/\eta_o$ in simulations.

2.3 Adhesive interactions

We employ adhesive bond dynamics between the cell membrane and the substrate. Ligands are distributed on a square lattice at the substrate with equal spacing $\delta x = \delta y = 0.3a$. All membrane vertices act as receptors. For each time step Δt_{md}, new bonds can be formed and existing bonds can dissociate. Each receptor

Published on 19 June 2019. Downloaded by Ruprecht-Karls Universitat Heidelberg on 6/27/2019 10:20:37 AM.

binds to the nearest ligand at the substrate with a constant on-rate κ_{on}, whenever the distance between them is smaller than the critical distance of $r_{cd} = 0.38a$. Every existing bond can break with a force dependent off-rate $\kappa_{off} = \kappa^0_{off}\exp(F/F_d)$ according to Bell's model.[42] Here, F_d is the internal force scale, which is determined to be about 10 pN for a PfEMP-1:CD36 bond.[43] In addition, each bond breaks if its length becomes larger than $2r_{cd}$, to avoid non-physically large bond extensions. For receptor–ligand bonds, we employ a harmonic force model:[11,24] $F(\ell) = k_s(\ell - r_0)$, where r_0 is the bond's equilibrium length. At each time step, new bonds are formed between possible partners with a probability $P_{on} = 1 - \exp(-\kappa_{on}\Delta t_{md})$ or existing bonds break with a probability $P_{off} = 1 - \exp(-\kappa_{off}\Delta t_{md})$. On- and off-rates are chosen to be shear-rate $\dot\gamma$ dependent such that $\kappa_{on}/\dot\gamma = 0.5$ and $\kappa^0_{off}/\dot\gamma = 0.5$. Even though such a choice introduces shear dependence for both the pre-factor and exponential force term in the Bell's model, the exponential force term dominates at all shear rates.

2.4 Simulation setup and parameters

All flow simulations are performed in a domain of size $50a \times 25a \times 25a$ with $a \simeq 0.81$ μm. Periodic boundary conditions are employed along the x (flow) and y (vorticity) directions, whereas hard-wall boundary conditions are employed in the z (flow gradient) direction. Solvent particles are reflected from the walls using bounce-back collisions, which are insufficient for achieving no-slip boundary conditions at the walls, and are therefore complemented by adding ghost particles within the wall layers of thickness a.[44] Since the collision step requires not only velocities but also positions of the particles, ghost particles within the walls are generated explicitly and their positions are drawn randomly from a uniform distribution. To generate shear flow, ghost particles are assigned a velocity $\boldsymbol{v} = \dot\gamma z\mathbf{e}_x$, resulting in a required shear rate $\dot\gamma$. In all simulations, the shear rate is characterized by a dimensionless shear rate,

$$\dot\gamma^* = \dot\gamma\tau = \dot\gamma\frac{\eta_o D_r^3}{\kappa_c}, \tag{12}$$

where $\tau = \eta_o D_r^3/\kappa_c$ is the characteristic relaxation time of a RBC. Stiffness of the cell is represented by the Föppl–von Kármán number,

$$\Gamma = \frac{4\mu_0 D_r^2}{\kappa_c} \simeq \frac{YD_r^2}{\kappa_c}, \tag{13}$$

since $Y \simeq 4\mu_0$ for a nearly incompressible membrane considered here.

To connect model units of all relevant parameters to physical units, we match corresponding length, force, and time scales.[31] The key parameters used in simulations are shown in Table 1. Furthermore, we employ the particle number density of $\rho = 25/a^3$ for both internal and external fluids. The mass of each membrane vertex is set to $M = \rho a^3 m$. The RBC shape is chosen to be discocyte with a reduced volume of about 0.64 and an effective size $D_r = \sqrt{A_0/\pi} \simeq 8.1a$. Even though the shape of iRBCs is significantly affected during intra-erythrocytic parasite development, iRBCs retain their nearly discoid shape with a small parasite bump at the side until trophozoite stage.[18] To eliminate inertial effects, we choose flow parameters such that the Reynolds number is always less than unity. For a typical value of shear rate $\dot\gamma = 0.3\sqrt{k_BT/ma^2}$, the Reynolds number becomes $\mathrm{Re} = D_r^2\dot\gamma\rho/4\eta_0 \simeq 0.4$. In simulations, only the shear modulus μ_0 is varied in order to alter the membrane stiffness, whereas the bending modulus is kept constant with $\kappa_c = 70k_BT = 3 \times 10^{-19}$ J. As initial condition, the cell is placed close to the wall at a distance of $a/8$ (or about 100 nm) and let to adhere. Then, the flow is started and the analysis of RBC behavior is performed after a time of 6.5τ to make sure that the cell has reached a steady adhesive dynamics.

Table 1 Simulation parameters in model and physical units. In simulations, length is measured in units of the lattice constant a, energy in units of k_BT and the time in units of $\sqrt{ma^2/k_BT}$. In all simulations, we select $a = 1$, $m = 1$, $k_BT = 0.1$ and $\Delta t_{cd} = 0.0032\sqrt{ma^2/k_BT}$

Parameters	Model units	Physical units
Lattice constant, a		0.81 μm
Membrane area, A_0	$205.2a^2$	134 μm^2
iRBC diameter, $D_r = \sqrt{A_0/\pi}$	$8.1a$	6.5 μm
Shear modulus, μ_0	$770k_BT/a^2$	5 μN m^{-1}
Bending modulus, κ_c	$70k_BT$	3×10^{-19} J
Plasma viscosity, η_o	$310\sqrt{mk_BT}/a^2$	1 mPa s
RBC relaxation time, $\tau = \eta_o D_r^3/\kappa_c$	$2337\sqrt{ma^2/k_BT}$	0.93 s
RBC volume, V_0	$177a^3$	93 μm^3
Spring constant, k_s	$8000k_BT/a^2$	5.2×10^{-5} N m^{-1}
Force scale, F_d	$2000k_BT/a$	10 pN
Critical distance, r_{cd}	$0.38a$	310 nm
Ligand spacing, d	$0.375a$–$0.5a$	300–400 nm

3 Results

3.1 Distinct dynamic states

Adhesion dynamics of round cells in shear flow has extensively been explored in the past in the context of leukocytes or late stage malaria-infected blood cells using Stokesian dynamics.[7,24,45] In these studies, cell deformation was neglected, which is a fair assumption as leukocytes or late stage iRBCs are close to spherical in flows with physiologically relevant shear stresses. To ensure that a sufficiently large contact area can be formed in a non-deformable cell model, one has to allow for a large binding range. In order to study the effect of the contact area on cell adhesion in more detail, leukocyte deformability has explicitly been considered in adhesive dynamics simulations for round reference shapes.[12,13] However, for early or mid-stage iRBCs (rings or trophozoites), cell shape is still mainly biconcave and deformations around this shape have to be considered.[23,25]

The two major dynamic states that we observe are crawling and flipping. Fig. 1 presents snapshots of a cell, exhibiting crawling and flipping dynamics. Both trajectories are for the same shear rate, $\dot\gamma = 460$ Hz ($\dot\gamma^* \simeq 430$), but crawling is obtained for a RBC with a shear modulus of $\mu_0 = 5$ μN m^{-1} ($\Gamma \simeq 2870$), whereas flipping is shown for a cell with a shear modulus of $\mu_0 = 25$ μN m^{-1} ($\Gamma \simeq 14\,370$). The crawling state is characterized by a continuous membrane rotation and the cell's deformed

 This journal is © The Royal Society of Chemistry 2019

Published on 19 June 2019. Downloaded by Ruprecht-Karls Universitat Heidelberg on 6/27/2019 10:20:37 AM.

shape remains nearly unchanged, making a small angle with respect to the flow direction. In contrast, pure flipping does not have much membrane rotation, but cell shape undergoes strong changes in time. To quantify the both dynamic states, we measure different quantities which can help us distinguish these states, such as (1) inclination angle, (2) translational velocity, (3) deformation index (DI), and (4) contact area. The inclination angle is defined as the angle between the cell's long axis (in the flow *vs.* shear gradient plane) and the flow (or x) direction. To measure the orientational axis, we employ the gyration tensor given by

$$G_{ij} = (1/N)\sum_{k}^{N}\left(r_{i,k} - r_{i,c}\right)\cdot\left(r_{j,k} - r_{j,c}\right), \qquad (14)$$

where the summation runs over all membrane vertices, i and j stand for x, y, or z-components, and $r_{i,c}$ is the ith component of center of mass of the RBC. The cell's orientational axis is most reliably determined by the eigenvector with the smallest eigenvalue, because the choice of eigenvector that corresponds to the largest eigenvalue leads sometimes to an inconsistent cell orientation direction, as there are two similar major axes for discocytic shape of the RBC.

The deformation index is defined as DI = $|L - H|/(L + H)$, where L and H are maximum extensions of the cell in x and z directions, respectively. Fig. 2 shows all four measured quantities for the crawling and flipping states. The time-implicit plot of inclination angle *versus* deformation index in Fig. 2(a) shows that movements and deformations oscillate in a similar manner in both cases, but that they are much more pronounced in the case of flipping. Even though it captures the essential character of flipping, the eigenvector of the gyration tensor with the smallest eigenvalue does not always faithfully represent the orientation of a flipping RBC, as this dynamics involves complex cell deformations which may result in over- or underestimation of the inclination angle. The plots of RBC-velocity and contact area shown in Fig. 2(b) demonstrate that significant oscillations only exist in the flipping case, while the crawling case is characterized by essentially constant values of velocity and contact area. We also see that crawling has larger contact area and smaller velocity than flipping, and thus corresponds to stronger adhesion. For flipping, we see that velocity and contact area are out of phase by 180° as periodic cell deformations during flipping with low and higher contact zones correspond to high and lower velocities, respectively. The oscillatory nature of the translational velocity for the flipping motion has already been predicted in simulations[23] and further confirmed in flow chamber experiments.[24]

The other relevant adhesion states observed in simulations are firm adhesion and complete detachment from the wall. Firm adhesion is observed at low shear rates, while RBC detachment occurs mainly at high shear rates. These two states generally depend on the overall binding strength of the cell and shear stress exerted by the flow, but only mildly on the cell deformability. For this reason, these two states are also well known for leukocytes, whose adhesive state diagram is mainly governed by bond kinetics. Therefore, the positioning of these two states in the state diagram for iRBCs should resemble that of the adhesion diagram for leukocytes.[11] Different from leukocytes, cell rolling is not observed here due to the non-spherical (biconcave) shapes used in simulations for iRBCs. However, in the late (schizont) stage, iRBCs become spherical and can exhibit rolling motion.[24]

3.2 State diagram

Fig. 3 presents the central result of our study, the adhesive state diagram of iRBCs in shear flow. The diagram is plotted as a function of the dimensionless shear rate $\dot{\gamma}^*$ and the cell stiffness characterized by the Föppl–von Kármán number Γ. The range of dimensionless shear rates $\dot{\gamma}^* \in [100;1100]$ in Fig. 3 corresponds approximately to $\dot{\gamma} \in [110;1200]$ s^{-1} and shear stresses from 0.1 Pa to 1.2 Pa, which mainly span typical conditions in venules. Cell stiffness is varied by changing the shear modulus μ_0 from 5 μN m^{-1} ($\Gamma \simeq 2870$), which is the average value for a healthy RBC (see Table 1), to 35 μN m^{-1} ($\Gamma \simeq 20\,120$), representing the stage of a late trophozoite.[19] Here, the viscosity contrast $\lambda = \eta_i/\eta_o$ between internal and external fluids is set to unity. Note that the state diagram in

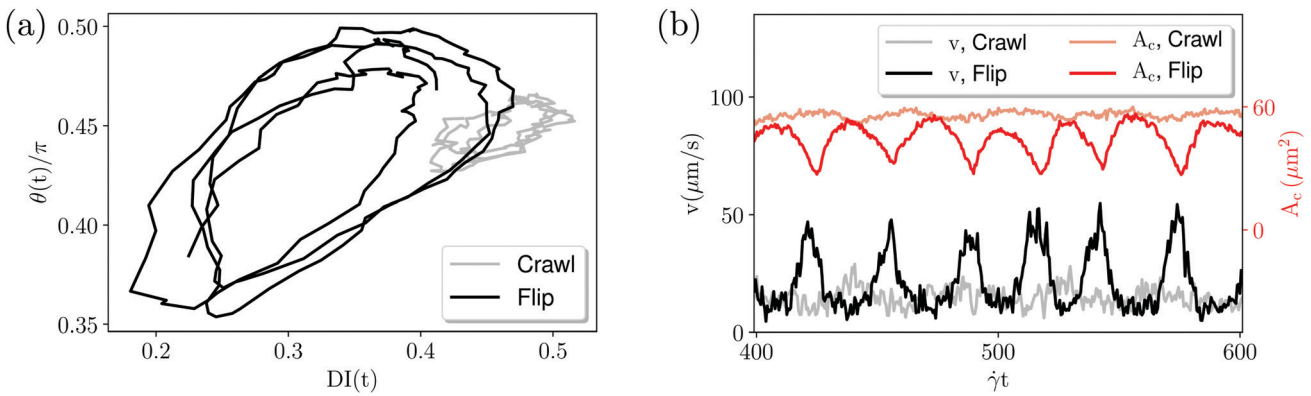

Fig. 2 (a) Time-implicit plot of inclination angle $\theta(t)$ *versus* deformation index DI(t) and (b) velocity v (left y-axis) and contact area A_c (right y-axis) against dimensionless time $\dot{\gamma}t$ are shown for representative trajectories of crawling and flipping motion. The shear rate is $\dot{\gamma}$ = 460 Hz ($\dot{\gamma}^* \simeq 430$) in both cases. Crawling and flipping motion is for cells with a shear modulus of μ_0 = 5 μN m^{-1} ($\Gamma \simeq 2870$) and μ_0 = 25 μN m^{-1} ($\Gamma \simeq 14\,370$), respectively.

Published on 19 June 2019. Downloaded by Ruprecht-Karls Universitat Heidelberg on 6/27/2019 10:20:37 AM.

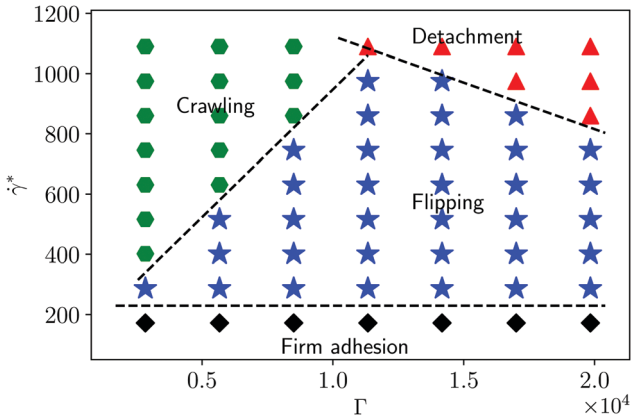

Fig. 3 Adhesive state diagram for the viscosity contrast $\lambda = 1$ as a function of dimensionless cell stiffness characterized by the Föppl–von Kármán number Γ and the dimensionless shear rate $\dot{\gamma}^*$. The state diagram comprises the dynamic states: crawling (green hexagons), flipping (blue stars), firm adhesion (black diamonds), and free motion (red triangles). Dashed lines between the states are drawn schematically for visual guidance.

Fig. 3 is simulated for a shear-dependent on-rate $\kappa_{on}/\dot{\gamma} = 0.5$ and off-rate $\kappa^0_{off}/\dot{\gamma} = 0.5$.

The state diagram in Fig. 3 shows that firm adhesion occurs at small shear rates, as expected. A state is considered to be firm adhesion whenever the average velocity of an iRBC is smaller than 5 μm s^{-1} (see Table 2). The detachment of iRBCs typically happens at high shear rates, but may also occur at moderate $\dot{\gamma}^*$ values for stiff cells (or large Γ). Occurrence of the other two states (*i.e.* crawling and flipping) strongly depends on the cell stiffness. In particular, the region of iRBC crawling widens in terms of the cell stiffness (quantified by Γ) with increasing shear rate. To uniquely identify the crawling and flipping states, we employ two measures: (i) deformation index DI and (ii) standard deviation σ_v of the cell velocity. Note that both quantities can also be measured easily in flow chamber experiments. Fig. 4 presents the deformation index and the standard deviation of velocity normalized by the average RBC velocity $\langle v \rangle$. $\sigma_v/\langle v \rangle$ in Fig. 4(a) varies between 0.1 and 0.8. For the crawling state, $\sigma_v/\langle v \rangle$ is generally small, as the iRBC exhibits relatively stable motion with a nearly constant velocity. In case of flipping, $\sigma_v/\langle v \rangle$ is always larger than 0.4 due to the oscillating behavior of iRBC velocity. Note that for iRBCs moving very slowly with a velocity of a few μm s^{-1}, σ_v characteristic is not very useful as they typically flip only 1–2 times over the whole time of observation. The deformation index in Fig. 4(b) does not change much and is close to 0.45 for the crawling state, whereas DI is less than 0.35 for flipping. For comparison,

Table 2 Criteria for the characterization of different dynamic states of iRBCs. U_{hd} is the free cell velocity close to the substrate

Definition	State
$\langle v \rangle < 5$ μm s^{-1}	Firm adhesion
$\sigma_v/\langle v \rangle < 0.4$ or DI > 0.42	Crawling
$\sigma_v/\langle v \rangle > 0.4$ or DI < 0.42	Flipping
$\langle v \rangle \simeq U_{hd}$	Detachment

deformation index of an undeformed biconcave RBC (diameter $d \simeq 8$ μm and height of $h \simeq 3$ μm) is close to DI $= (d - h)/(d + h) \simeq 0.45$. During flipping motion, the iRBC experiences repeated dynamics with strong shape deformations (see snapshots in Fig. 1(b)), which results in DI to oscillate between 0.2 and 0.5 (see Fig. 2(a)) with an average value close to 0.3. Therefore, by selecting threshold values for these two characteristics (0.4 for $\sigma_v/\langle v \rangle$ and 0.42 for DI), as shown in Table 2, both the crawling and flipping states can be uniquely distinguished. In fact, the conditions in Table 2 were already used to determine various adhesive states in simulations and construct the state diagram in Fig. 3. Note that changes in bond properties, such as the spring constant and bond kinetic rates, will affect boundaries between different adhesive states, but the overall diagram structure is expected to be qualitatively similar to that presented in Fig. 3.

3.3 Effect of viscosity contrast

Viscosity contrast λ between internal and external fluids strongly affects the dynamics of vesicles[46–48] and RBCs[35,49,50] in shear flow. Here, the role of viscosity contrast on adhesion dynamics is investigated. A larger viscosity of the internal fluid is introduced by increasing the mass of fluid particles inside the RBC, since the collisional part of viscosity in MPCD depends linearly on the particle mass while the kinetic part can be neglected for small collision timesteps (see eqn (3)). This implies that the viscosity contrast $\lambda = \eta_i/\eta_o \simeq m_i/m_o$. For a healthy RBC, cytosol viscosity is found to be about 5 mPa s at room temperature,[51] although it may change for different temperatures.[52] Thus, the typical viscosity contrast for healthy RBCs is $\lambda = 5$. For iRBCs, the presence of parasite is expected to further increase the viscosity contrast due to the parasite-induced generation of new structures inside iRBCs.

Fig. 5(a) shows average velocities of the cell as a function of dimensionless shear rate $\dot{\gamma}^*$ for three viscosity contrasts $\lambda = 1$, 10, and 20. The cell's shear modulus is $\mu_0 = 5$ μN m^{-1} ($\Gamma \simeq 2870$) in all cases, ensuring that the RBC remains in the crawling state. We find that the adhesive behavior of a RBC is qualitatively similar for all viscosity contrasts; however, an increase in the viscosity contrast leads to a slight decrease in the cell's translational velocity. For crawling dynamics, an increase in the viscosity contrast affects two characteristics, resulting in (i) a decrease of the membrane's rotational speed and (ii) a slight change in the average inclination angle. The decrease in membrane rotational speed arises from an increased dissipation inside the RBC due to an increased internal viscosity. A further significant increase in the internal viscosity is likely to eventually prohibit the crawling motion and initiate flipping. An increase in λ also leads to a decrease in the average inclination angle, *i.e.*, the cell lies more flat on the substrate. For $\lambda = 1$, the average inclination angle is $\langle \theta \rangle \simeq 10^\circ$, while for $\lambda = 20$ it becomes $\langle \theta \rangle \simeq 7^\circ$. For a tank-treading RBC in simple shear flow, Keller–Skalak[46] or similar theories[53,54] also predict that the inclination angle decreases with increasing viscosity contrast until the RBC eventually stops tank-treading and starts to tumble like a rotating solid body. Fig. 5(b) presents the adhesive state diagram for the viscosity contrast

This journal is © The Royal Society of Chemistry 2019

Published on 19 June 2019. Downloaded by Ruprecht-Karls Universitat Heidelberg on 6/27/2019 10:20:37 AM.

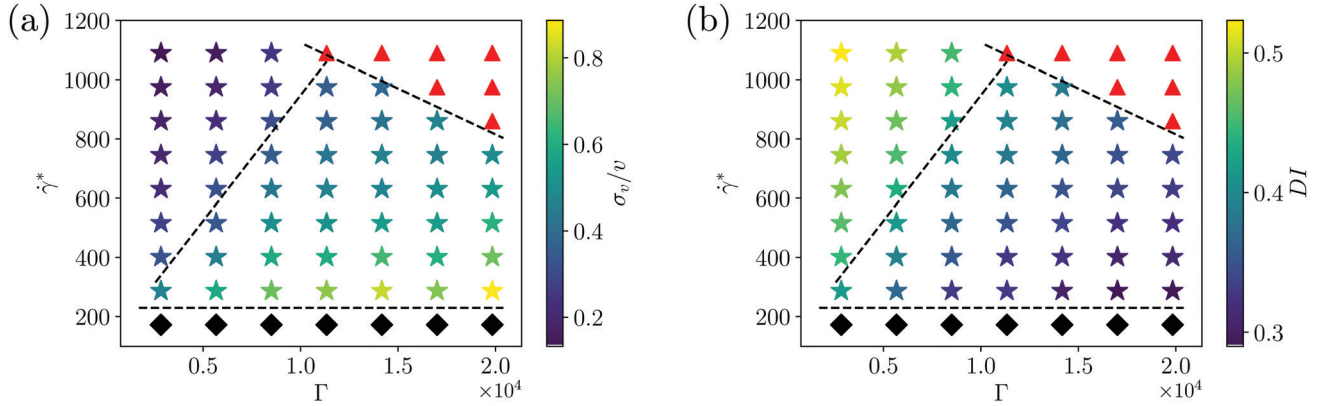

Fig. 4 (a) Standard deviation σ_v of RBC velocity and (b) deformation index as a function of the dimensionless shear rate $\dot{\gamma}^*$ and Föppl–von Kármán number Γ. The red triangles representing the detachment state and black diamonds corresponding to firm adhesion are excluded from the colormap. Dashed lines indicate schematically the boundaries between different adhesive states, and are identical to those in Fig. 3.

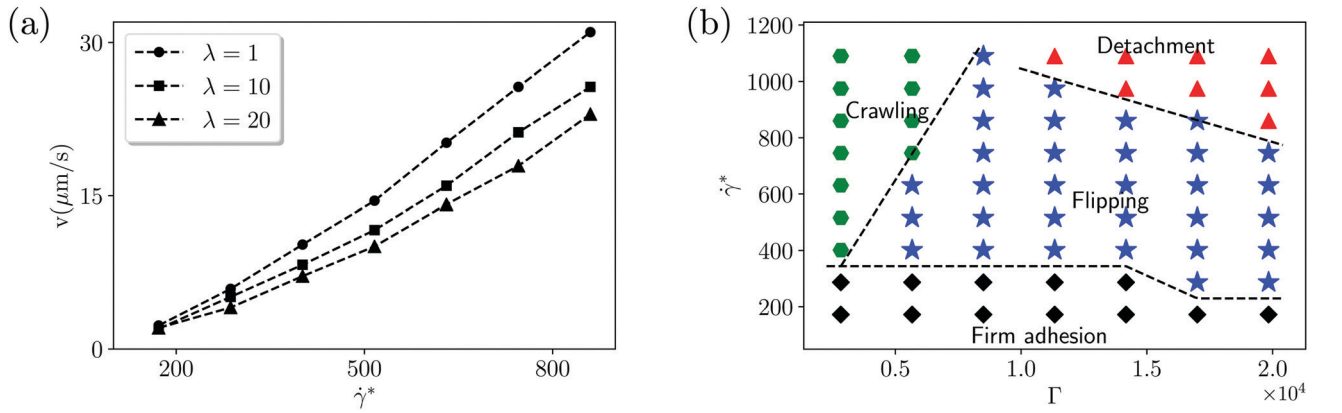

Fig. 5 (a) Mean translational velocities as a function of the dimensionless shear rate for three viscosity contrasts λ = 1, 10, and 20. The shear modulus of the cell is μ_0 = 5 μN m^{-1} ($\Gamma \simeq 2870$). (b) Adhesive state diagram for λ = 20, while all other parameters are kept same as for λ = 1 in Fig. 3. Different dynamic states are crawling (green hexagons), flipping (blue stars), firm adhesion (black diamonds), and free motion (red triangles). Dashed lines between the states are drawn schematically for visual guidance.

λ = 20. Interestingly, this state diagram is quite similar to that in Fig. 3 for λ = 1. Two notable differences in the state diagram for λ = 20 in comparison to that for λ = 1 are (i) an expansion of the firm-adhesion region toward larger shear rates and (ii) a reduction of the crawling region in favor of the flipping state. These changes in the state diagram are due to an increased dissipation with increasing viscosity contrast, such that membrane dynamics slows down, favoring RBC flipping and firm adhesion. Therefore, under certain conditions (*e.g.* close to the crawling-to-flipping transition) an increase in the viscosity contrast may initiate a transition from crawling to flipping dynamics.

4 Discussion and conclusions

Motivated by malaria-infected RBCs, we have systematically studied the adhesion dynamics of RBCs in shear flow, using mesoscale hydrodynamics simulations and a model of the RBC membrane with bending and stretching elasticity. Our main result is a state diagram which spans a wide range of shear rates and Föppl–von Kármán numbers, and comprises four adhesive dynamic states: firm adhesion, crawling, flipping and detachment, depending upon the cell stiffness and applied shear rate. We have shown that RBCs generally crawl at high shear stresses and flip at low shear stresses. The critical shear stress that defines this transition increases with the membrane shear stiffness.

Our simulations predict that healthy RBCs would crawl for nearly all shear rates if they were adhesive. However, in contrast to white blood cells, they are not adhesive, and only become so during a malaria infection. Once iRBCs become sufficiently adhesive so that they show significant adhesive interactions with the substrate, they are already so stiff that they exhibit flipping. In recent flow chamber experiments,[24,55] iRBCs at the trophozoite stage were indeed shown to flip at shear stresses in the range of 0.03–0.1 Pa. Even though at high enough shear stresses, crawling of trophozoites should theoretically be possible, this would require high enough ligand densities to avoid cell detachment. Therefore, our conclusion is that an increased cell stiffness (*i.e.* shear modulus) is the main mechanism that

Published on 19 June 2019. Downloaded by Ruprecht-Karls Universitat Heidelberg on 6/27/2019 10:20:37 AM.

Table 3 Distinct dynamic states for mid-stage iRBCs and late-stage iRBCs for various parameter regimes as predicted from our simulation results. Note that late-stage iRBCs resemble leukocytes

Conditions	Mid-stage iRBC	Late-stage iRBC
Low $\dot{\gamma}$	Firm adhesion	Firm adhesion
Moderate $\dot{\gamma}$ & Γ or moderate $\dot{\gamma}$ & κ_{on}	Flipping	Rolling adhesion
High $\dot{\gamma}$ & low Γ or high $\dot{\gamma}$ & low κ_{on}	Crawling	Transient adhesion
Very high $\dot{\gamma}$	Detachment	Detachment

determines the flipping motion of iRBCs, which is consistent with a similar conclusion in ref. 23. In case of spherical cells such as leukocytes, an increase in shear stress always leads to an unstable rolling state such as transient adhesion or detachment state, whereas for non-spherical iRBCs, it generally results in stable adhesion states. Nevertheless, at very high shear stresses, hydrodynamic lift forces dominate over adhesion and would detach cells from the substrate in any case. Table 3 summarizes the predicted conditions which describe the different states for both leukocytes and iRBCs.

Crawling dynamics is qualitatively similar to tank-treading of vesicles and RBCs in simple shear flow. Tank-treading of vesicles and RBCs has been studied extensively both in experiments[32,33,54,56,57] and numerical simulations.[35,50,58–62] A theoretical model for vesicle dynamics was first proposed by Keller and Skalak,[46] where a fluid-filled particle with a fixed ellipsoidal shape in simple shear flow was considered. This model was further extended by others[53,54] by adding an additional elastic-energy barrier for membrane rotation, which represents the effect of shape memory for RBCs due to spectrin network elasticity.[63] The extended model predicts tumbling at low shear rates as an unsteady solid-like rotation and tank-treading at high shear rates, resembling the motion of a droplet in shear flow. The elastic-energy barrier for membrane rotation (or shape memory of a RBC) determines the tumbling-to-tank-treading transition for RBCs.

The underlying physical mechanism for the flipping-to-crawling transition is the same as that for the tumbling-to-tank-treading transition, except that the adhesion to a substrate alters the free-flow situation and leads to an additional friction for the membrane rotation. Dissimilar to the RBC adhesive behavior, which shows flipping at low shear rates and crawling at high shear rates, is the existence of other RBC dynamics and shapes (*e.g.* swinging, rolling, trilobes) in free shear flow besides tumbling and tank-treading.[35,50,54,57,64] From the adhesive state diagram in Fig. 3, the threshold value of shear rate for flipping-to-crawling transition increases linearly with the cell stiffness characterized by the Föppl–von Kármán number Γ. For instance, for RBC with a shear modulus of $\mu_0 = 5\ \mu N\ m^{-1}$ ($\Gamma \simeq 2870$) the threshold shear rate is $\dot{\gamma}^* \simeq 300$, whereas for $\mu_0 = 15\ \mu N\ m^{-1}$ ($\Gamma \simeq 8620$), the threshold value is about $\dot{\gamma}^* \simeq 800$. However, the boundary between crawling and flipping states is not very sharp. In the state diagram, the points that are close to the crawling-to-flipping boundary may possess both flipping and crawling characteristics at the same time. For example, a flipping cell may exhibit a non-zero membrane rotation, while a crawling RBC may occasionally flip near the transition.

Viscosity contrast between internal and external fluids plays an important role for RBC dynamics in free shear flow.[35,49,50] For example, a high enough viscosity contrast suppresses tank-treading at high shear rates and generally leads to multilobe dynamics. For the adhesion of iRBCs, we find that the effect of viscosity contrast λ is relatively weak, even for such high values as $\lambda = 20$. Similar to an increase in membrane shear modulus, a high viscosity contrast stabilizes the flipping state. Therefore, we conclude that the simultaneous increase in shear modulus and viscosity contrast occurring for iRBCs enforces flipping and not crawling dynamics of infected cells. Crawling of iRBCs is expected for conditions of strong adhesion, which in fact may potentially occur locally *in vivo*.

Even though our model system is inspired by mid-stage malaria-infected RBCs, we employ only a few specific assumptions, making our study general enough for the wall adhesion of biconcave capsules in shear flow. The assumption of discocytic RBC shape is fair enough up to mid-trophozoite stage, after which an iRBCs changes toward a spherical shape.[18] Our simulations have shown that changes in shear modulus and viscosity contrast have important effects on the cell dynamics and its adhesive interactions with the substrate. In the future, it would be interesting to consider the effect of an inhomogeneous knob density at the surface of iRBCs on their adhesive dynamics, since the knob density is not constant and changes during different parasite development stages.[65] Furthermore, one might consider to go beyond single-cell adhesion and investigate wall binding of iRBCs in blood flow at higher densities of both RBCs and iRBCs, and also with other blood components being present.

Conflicts of interest

There are no conflicts to declare.

Acknowledgements

This project was partially funded by the Deutsche Forschungsgemeinschaft (DFG, German Research Foundation) with project number 240245660 (SFB 1129 to U.S.S.). A. K. D. and U. S. S. acknowledge computer support by the state of Baden-Württemberg through bwHPC. A. K. D. would like to thank Falko Ziebert for helpful discussions. U. S. S. is a member of the cluster of excellence CellNetworks and of the Interdisciplinary Center for Scientific Computing (IWR) at Heidelberg.

 This journal is © The Royal Society of Chemistry 2019

Published on 19 June 2019. Downloaded by Ruprecht-Karls Universitat Heidelberg on 6/27/2019 10:20:37 AM.

Notes and references

1 T. A. Springer, *Annu. Rev. Physiol.*, 1995, **57**, 827–872.
2 L. H. Miller, D. I. Baruch, K. Marsh and O. K. Doumbo, *Nature*, 2002, **415**, 673–679.
3 D. A. Hammer, *J. Biomech. Eng.*, 2014, **136**, 021006.
4 M. B. Lawrence and T. A. Springer, *Cell*, 1991, **65**, 859–873.
5 R. Alon, D. A. Hammer and T. A. Springer, *Nature*, 1995, **374**, 539–542.
6 B. T. Marshall, M. Long, J. W. Piper, T. Yago, R. P. McEver and C. Zhu, *Nature*, 2003, **423**, 190.
7 D. A. Hammer and S. M. Apte, *Biophys. J.*, 1992, **63**, 35.
8 K.-C. Chang, D. F. Tees and D. A. Hammer, *Proc. Natl. Acad. Sci. U. S. A.*, 2000, **97**, 11262–11267.
9 K. E. Caputo and D. A. Hammer, *Biophys. J.*, 2005, **89**, 187–200.
10 C. Korn and U. S. Schwarz, *Phys. Rev. Lett.*, 2006, **97**, 138103.
11 C. Korn and U. Schwarz, *Phys. Rev. E: Stat., Nonlinear, Soft Matter Phys.*, 2008, **77**, 041904.
12 S. Jadhav, C. D. Eggleton and K. Konstantopoulos, *Biophys. J.*, 2005, **88**, 96–104.
13 Z. Y. Luo and B. F. Bai, *Soft Matter*, 2016, **12**, 6918–6925.
14 G. Helms, A. K. Dasanna, U. S. Schwarz and M. Lanzer, *FEBS Lett.*, 2016, **590**, 1955–1971.
15 J. Gruenberg, D. R. Allred and I. W. Sherman, *J. Cell Biol.*, 1983, **97**, 795–802.
16 E. Nagao, O. Kaneko and J. A. Dvorak, *J. Struct. Biol.*, 2000, **130**, 34–44.
17 A. Esposito, J.-B. Choimet, J. N. Skepper, J. M. Mauritz, V. L. Lew, C. F. Kaminski and T. Tiffert, *Biophys. J.*, 2010, **99**, 953–960.
18 M. Waldecker, A. K. Dasanna, C. Lansche, M. Linke, S. Srismith, M. Cyrklaff, C. P. Sanchez, U. S. Schwarz and M. Lanzer, *Cell. Microbiol.*, 2017, **19**, e12650.
19 J. Li, M. Dao, C. Lim and S. Suresh, *Biophys. J.*, 2005, **88**, 3707–3719.
20 B. G. Yipp, S. Anand, T. Schollaardt, K. D. Patel, S. Looareesuwan and M. Ho, *Blood*, 2000, **96**, 2292–2298.
21 B. M. Cooke, A. R. Berendt, A. G. Craig, J. MacGregor, C. I. Newbold and G. B. Nash, *Br. J. Haematol.*, 1994, **87**, 162–170.
22 M. Antia, T. Herricks and P. K. Rathod, *PLoS Pathog.*, 2007, **3**, e99.
23 D. Fedosov, B. Caswell and G. Karniadakis, *Biophys. J.*, 2011, **100**, 2084–2093.
24 A. K. Dasanna, C. Lansche, M. Lanzer and U. S. Schwarz, *Biophys. J.*, 2017, **112**, 1908–1919.
25 C. Lansche, A. K. Dasanna, K. Quadt, B. Fröhlich, D. Missirlis, M. Tétard, B. Gamain, B. Buchholz, C. P. Sanchez and M. Tanaka, *et al.*, *Commun. Biol.*, 2018, **1**, 211.
26 A. K. Dasanna, U. S. Schwarz, G. Gompper and D. A. Fedosov, *Handbook of Materials Modeling: Applications: Current and Emerging Materials*, 2018, pp. 1–24.
27 A. Malevanets and R. Kapral, *J. Chem. Phys.*, 1999, **110**, 8605–8613.
28 G. Gompper, T. Ihle, D. Kroll and R. Winkler, *Advanced computer simulation approaches for soft matter sciences III*, Advances in Polymer Science, Springer, 2009, vol. 221, pp. 1–87.
29 G. Gompper and D. M. Kroll, *Statistical Mechanics of Membranes and Surfaces*, World Scientific, Singapore, 2nd edn, 2004, ch. 12, pp. 359–426.
30 H. Noguchi and G. Gompper, *Proc. Natl. Acad. Sci. U. S. A.*, 2005, **102**, 14159–14164.
31 D. A. Fedosov, B. Caswell and G. E. Karniadakis, *Biophys. J.*, 2010, **98**, 2215–2225.
32 T. M. Fischer, M. Stohr-Lissen and H. Schmid-Schonbein, *Science*, 1978, **202**, 894–896.
33 M. Abkarian and A. Viallat, *Soft Matter*, 2008, **4**, 653–657.
34 M. Wilczek, W. Tewes, S. Engelnkemper, S. V. Gurevich and U. Thiele, *Phys. Rev. Lett.*, 2017, **119**, 204501.
35 L. Lanotte, J. Mauer, S. Mendez, D. A. Fedosov, J.-M. Fromental, V. Claveria, F. Nicoud, G. Gompper and M. Abkarian, *Proc. Natl. Acad. Sci. U. S. A.*, 2016, **113**, 13289–13294.
36 H. Noguchi, N. Kikuchi and G. Gompper, *EPL*, 2007, **78**, 10005.
37 I. O. Götze, H. Noguchi and G. Gompper, *Phys. Rev. E: Stat., Nonlinear, Soft Matter Phys.*, 2007, **76**, 046705.
38 H. Noguchi and G. Gompper, *Phys. Rev. E: Stat., Nonlinear, Soft Matter Phys.*, 2008, **78**, 016706.
39 D. A. Fedosov, B. Caswell and G. E. Karniadakis, *Comput. Meth. Appl. Mech. Eng.*, 2010, **199**, 1937–1948.
40 I. V. Pivkin and G. E. Karniadakis, *Phys. Rev. Lett.*, 2008, **101**, 118105.
41 W. Helfrich, *Z. Naturforsch., C: J. Biosci.*, 1973, **28**, 693–703.
42 G. I. Bell, *Science*, 1978, **200**, 618–627.
43 Y. B. Lim, J. Thingna, J. Cao and C. T. Lim, *Sci. Rep.*, 2017, **7**, 4208.
44 A. Lamura, G. Gompper, T. Ihle and D. Kroll, *Europhys. Lett.*, 2001, **56**, 319.
45 C. B. Korn and U. S. Schwarz, *J. Chem. Phys.*, 2007, **126**, 9.
46 S. R. Keller and R. Skalak, *J. Fluid Mech.*, 1982, **120**, 27–47.
47 H. Noguchi and G. Gompper, *Phys. Rev. E: Stat., Nonlinear, Soft Matter Phys.*, 2005, **72**, 011901.
48 V. Vitkova, M.-A. Mader, B. Polack, C. Misbah and T. Podgorski, *Biophys. J.*, 2008, **95**, L33–L35.
49 D. Cordasco, A. Yazdani and P. Bagchi, *Phys. Fluids*, 2014, **26**, 041902.
50 J. Mauer, S. Mendez, L. Lanotte, F. Nicoud, M. Abkarian, G. Gompper and D. A. Fedosov, *Phys. Rev. Lett.*, 2018, **121**, 118103.
51 R. Wells and H. Schmid-Schönbein, *J. Appl. Physiol.*, 1969, **27**, 213–217.
52 C. Kelemen, S. Chien and G. Artmann, *Biophys. J.*, 2001, **80**, 2622–2630.
53 J. Skotheim and T. W. Secomb, *Phys. Rev. Lett.*, 2007, **98**, 078301.
54 M. Abkarian, M. Faivre and A. Viallat, *Phys. Rev. Lett.*, 2007, **98**, 188302.
55 V. Introini, A. Carciati, G. Tomaiuolo, P. Cicuta and S. Guido, *J. R. Soc., Interface*, 2018, **15**, 20180773.
56 T. M. Fischer, *Biophys. J.*, 1980, **32**, 863.
57 J. Dupire, M. Socol and A. Viallat, *Proc. Natl. Acad. Sci. U. S. A.*, 2012, **109**, 20808–20813.

Published on 19 June 2019. Downloaded by Ruprecht-Karls Universitat Heidelberg on 6/27/2019 10:20:37 AM.

58 C. Pozrikidis, *Ann. Biomed. Eng.*, 2003, **31**, 1194–1205.
59 A. Z. Yazdani and P. Bagchi, *Phys. Rev. E: Stat., Nonlinear, Soft Matter Phys.*, 2011, **84**, 026314.
60 Y. Sui, Y. Chew, P. Roy, Y. Cheng and H. Low, *Phys. Fluids*, 2008, **20**, 112106.
61 H. Noguchi and G. Gompper, *Phys. Rev. Lett.*, 2004, **93**, 258102.
62 C. Misbah, *J. Phys.: Conf. Ser.*, 2012, 012005.
63 T. M. Fischer, *Biophys. J.*, 2004, **86**, 3304–3313.
64 H. Noguchi and G. Gompper, *Phys. Rev. Lett.*, 2007, **98**, 128103.
65 K. A. Quadt, L. Barfod, D. Andersen, J. Bruun, B. Gyan, T. Hassenkam, M. F. Ofori and L. Hviid, *PLoS One*, 2012, **7**, 1–8.

 This journal is © The Royal Society of Chemistry 2019